Journal of Volcanology and Geothermal Research xxx (2009) xxx–xxx

Contents lists available at ScienceDirect

Journal of Volcanology and Geothermal Research

journal homepage: www.elsevier.com/locate/jvolgeores

# P-wave velocity structure of Piton de la Fournaise volcano deduced from seismic data recorded between 1996 and 1999

Elodie Prôno [a], Jean Battaglia [a,*], Vadim Monteiller [b], Jean-Luc Got [b], Valérie Ferrazzini [c]

[a] Laboratoire Magmas et Volcans, Observatoire de Physique du Globe de Clermont , CNRS, 5 rue Kessler, 63000 Clermont-Ferrand, France
[b] LGIT, CNRS, Université de Savoie, Le Bourget-du-Lac 73376, France
[c] Observatoire Volcanologique du Piton de la Fournaise, Institut de Physique du Globe de Paris, 14 RN3, 97148, La Plaine des Cafres, France

ARTICLE INFO

*Article history:*
Received 7 April 2008
Accepted 4 December 2008
Available online xxxx

*Keywords:*
seismic tomography
structure
Piton de la Fournaise

ABSTRACT

Piton de la Fournaise is a highly active basaltic volcano located on La Réunion island. With the aim of gaining information on its 3D internal structure, we carried out a 3D tomographic inversion based on P-wave first arrival times for earthquakes recorded by the local seismic monitoring network of the Observatoire Volcanologique du Piton de la Fournaise (OVPF). We used data recorded between 1996 and 1999 during inter-eruptive periods as well as during the pre-eruptive swarms which preceded the eruptions in March 1998, July and September 1999. Volcano-tectonic activity below the volcano is mostly located at shallow depth, above sea level and below the central cone. However, the seismic crisis which preceded the March 9, 1998 eruption included a large number of events at greater depth providing an unprecedented data set which sheds light on the deep structure of the volcano. The tomographic technique which we used is based on an accurate finite-difference travel-time computation and a simultaneous probabilistic inversion of both velocity models and earthquake locations. The inversion is carried out using an improved technique which allows to well constrain the inversion parameters. This processing provides high quality stable tomographic images.

The obtained P-wave velocity model confirms the presence of a high-velocity plug above sea level, under the summit craters. This anomaly is interpreted as corresponding to an intrusive, solidified dyke-and-sill complex with little fluid magma storage. The high number of hypocenters in the zone above sea level accounts for massive rock fracturing when magma rises toward the surface. The shallow high velocity plug is surrounded by a low-velocity ring known as being fractured and vesicular lavas or scorias located on volcano flanks. Two low-velocity anomalies are found below the summit caldera. The most superficial spreads from 1 km to 0 a.s.l.. The second is located below 1 km b.s.l.. These volumes may correspond to magma storage systems. They are separated by a relatively high velocity volume at sea level with a strong velocity gradient reaching 0.6 km/s per km.



## 1. Introduction

Seismic tomography is a major tool allowing to gain information on the structure below the ground surface through the assessment of the propagation velocity of seismic waves through the medium (Aki and Lee, 1976). It supplies an image of the structure based on the spatial distribution of seismic velocities obtained from earthquake travel times. The interest of the method relies in the fact that the velocities are representative of the physical properties of the medium which they cross. However, these velocities can be modified by various physico-chemical factors such as variations of ambient temperature and pressure, the nature of rocks and mineral phases, the degree and type of fracturing of the environment, the stress field, the porosity or the degree of saturation in fluids (Vanorio et al., 2005; Alfaro et al., 2007).

In the case of volcanoes, velocity variations can be due to contrasts of density or differences of rheology existing between melted rocks in the magmatic reservoir, and the surrounding rocks. Waves will propagate faster in dense materials such as magmatic intrusive complexes (Nercessian et al., 1996), solidified dykes, deposits of massive lava flows (Molina et al., 2005) or hardened and strengthened tuffs (Benz et al., 1996). Velocities will be lower if rocks are highly fractured or hydrothermally and chemically alterated (Benz et al., 1996; Garcia-Aristizabal et al., 2007), if there are volcanoclastic deposits which are not strengthened, less dense and porous (Molina et al., 2005; Alfaro et al., 2007), if the temperature is high or if there is a strong proportion of magma in the structure (Nercessian et al., 1996). Therefore tomography on volcanoes is a useful tool to identify major geological structures such as fluid storage systems and intrusive complexes.

At Piton de la Fournaise the velocity structure is mostly known on a fine scale for areas below the summit of the volcano and above sea level (Nercessian et al., 1996). This is mainly due to the very small number of events recorded below sea level since the installation of the OVPF in 1980 and prior to the March 1998 eruption. Indeed during this

* Corresponding author.
*E-mail address:* battag@opgc.univ-bpclermont.fr (J. Battaglia).

0377-0273/$ – see front matter © 2008 Elsevier B.V. All rights reserved.
doi:10.1016/j.jvolgeores.2008.12.009

whole period most of the seismicity was found above sea level and below the central cone with no or few deeper events which could be related to magma transfers at depth (Lénat and Bachèlery, 1990). Recently, Brenguier et al. (2007) used ambient noise to determine the surface-wave velocity structure, and therefore the S-wave velocity structure, of the shallow part of the edifice. On a larger scale, based on active shots, Gallart et al. (1999) provided a 2D P-wave velocity model for the entire island and surrounding oceanic crust, along a section passing north-west of the volcano.

The March 9, 1998 pre-eruptive crisis, which lasted for more than 36 h, included more than 3100 earthquakes with most of the events occurring below sea level. Their hypocenters describe a quasi-continuous way along which the activity migrated to the surface (Battaglia et al., 2005). This activity thus samples the zone located under the summit from 6 km below sea level up to the surface including areas showing previously no activity. This sampling is favorable for the investigation of seismic velocities below the summit caldera.

The purpose of this study is to obtain a new tomographic image of the Piton de la Fournaise volcano using the earthquakes recorded between 1996 and 1999. This work will allow us highlighting deeper zones of the volcano plumbing system as compared to previous works.

## 2. Geological settings

La Réunion island is a volcanic island located in the Indian Ocean (21°07'S–55°32'E), about 700 km east of Madagascar and 200 km southwest of Mauritius. It is related to the activity of a hot spot from which also arose the Mascareigne Plateau and Rodrigues and Mauritius islands. La Réunion island is the youngest island, its activity began about 5 My ago, and reached the surface about 2 My ago (Bonneville, 1990). The island is build on the oceanic floor at 4000 m depth where it has an average diameter of 220 km. Only 3% of its total volume appear above sea level. The island is 72 km long and 51 km wide, that is a surface of 2512 km$^2$, and is stretched out according to a direction N120°. It is composed of two shield volcanoes, the Piton des Neiges volcano, which is 3069 m high and the Piton de la Fournaise volcano, 2631 m.

Piton de la Fournaise is a basaltic volcano located in the southeastern part of the island. Its activity began 530000 years ago and is comparable to that of Hawaiian volcanoes, with periodic emissions of lava and sometimes more explosive eruptions. During the evolution of this volcano, three successive calderas formed, respectively, the Rivière des Remparts, the Rempart des Sables–Rivière de l'Est and the Rempart de Bellecombe (Gillot and Nativel, 1989). The most recent which corresponds to the Enclos Fouqué is about 5000 years old and is horse-shoe shaped and opened toward the sea at east. The summit of the Piton de la Fournaise is located in the Enclos Fouqué and is characterized by the presence of two craters: Bory in the west is smallest and now inactive and Dolomieu in the east which is the starting point of numerous recent eruptions, as well as the site of a major collapse in April 2007 (Michon et al., 2007). From the summit, two main radial fracture zones have been defined by Bachélery (1981) extending in the directions north 170 and 10°. Those fracture zones are interpreted as active rift zones.

The volcano is one of the most active in the world with a mean time between consecutive eruptions during the past two centuries of about 10 months (Stieltjes and Moutou, 1989). Most of the eruptions occur along fissures inside the Enclos Fouqué. From 1980 to 1992, 28 eruptions occurred, with most of them being only preceded by short duration seismic crises, including only earthquakes located above sea level. A pause in the activity was observed between 1992 and 1998 when the activity resumed with an eruption which lasted for more than 6 months. Since 1998 the eruptive activity is intense with 2 to 4 eruptions per year.

## 3. Data selection

The volcano is monitored since 1980 by the OVPF which is located 15 km from the summit and has permanent networks which monitor deformations, seismicity, magnetic field variations and Radon emissions. Campaign-style surveys complete these networks, including GPS measurements, gravimetry, electric resistivity and spontaneous polarization.

Seismic data used in our study were recorded by the permanent seismic network which included at that time 19 stations (Fig. 1) mostly located in the volcano area. Most of the stations are equipped with short period, one-component, 1-Hz vertical Mark Products L4 seismometers. Stations Bor, Pbr and TCR also include two horizontal components. At the time of our study, the data were recorded with a triggered mode and the acquisition was made with a sampling frequency of 100 Hz.

Our study is based on seismic events recorded between March 2, 1996 and September 28, 1999. We used data recorded during both inter-eruptive periods and during the pre-eruptive swarms which preceded the March 9, 1998 and July and September 1999 eruptions. Most of the eruptions of the Piton de la Fournaise are preceded by short pre-eruptive swarms of volcano-tectonic events located mainly above sea level, under the summit. The crisis which preceded the March 9, 1998 eruption is particular as it included a large number of earthquakes located below sea level and lasted for more than 36 h. Inter-eruptive seismicity mostly includes shallow earthquakes below the central cone.

Our initial database includes a total of 1110 volcano-tectonic events recorded by the 13 stations of the monitoring network situated in our tomography area with both P and S arrival times obtained by manually picking the waveforms. This set includes 229 events recorded in 1996 and 1997, 167 recorded in 1998 before the onset of the March 9 pre-eruptive swarm, 569 recorded during the swarm, 51 recorded in 1998 after the onset of the eruption and 94 earthquakes recorded mostly during the 2 pre-eruptive swarms which occurred in 1999. Preliminary locations were obtained using a modified version of the software HYPO71 (Lee and Lahr, 1975) adapted to take into account station elevations. For this purpose, we used a 1D velocity model used for routine location by the Observatory composed of 8 layers with velocities ranging from 3.5 km at the surface to 8.0 km/s at 30 km below sea level.

For this tomographic study we selected from the initial data set the best constrained events located inside our tomographic volume, with at least 6 phase pickings, a RMS time residual smaller than 0.2 s and an azimuthal GAP smaller than 180°. In the end, 861 events were retained (Fig. 2) providing 7965 P-wave arrival times. Due to the low coverage of stations with horizontal components where S waves can be identified reliably, we disregard S arrival times for tomography purpose and only present results for P-wave tomography.

## 4. Tomographic method

We performed a three-dimensional travel-time tomography using the probabilistic algorithm of Monteiller et al. (2005). Theoretical travel-times are computed using the Podvin-Lecomte finite-difference algorithm (Podvin and Lecomte, 1991) and a posteriori ray computation. Re-computation of travel-times along the ray allows to reach a relative accuracy better than $10^{-4}$ s.

Earthquake tomography belongs to a class of non-linear and ill-posed optimization problems whose solution has been discussed by Tarantola and Valette (1982) and Tarantola (1987). The tomographic problem should be written in a functional form

$$g(\mathbf{m}) = \mathbf{d} \quad (1)$$

where $g$ represents the functional used to solve the direct problem, $\mathbf{m}$ is the vector containing model parameters, and $\mathbf{d}$ the travel-time data. The purpose of the inverse problem is to find a model $\mathbf{m}$ fitting to best the measured data $\mathbf{d}$.

In the hypothesis that both data and model parameters have a gaussian distribution, Tarantola and Valette (1982) proposed for solving the inverse problem to minimize a cost function which is a

Please cite this article as: Prôno, E., et al., P-wave velocity structure of Piton de la Fournaise volcano deduced from seismic data recorded between 1996 and 1999, J. Volcanol. Geotherm. Res. (2009), doi:10.1016/j.jvolgeores.2008.12.009

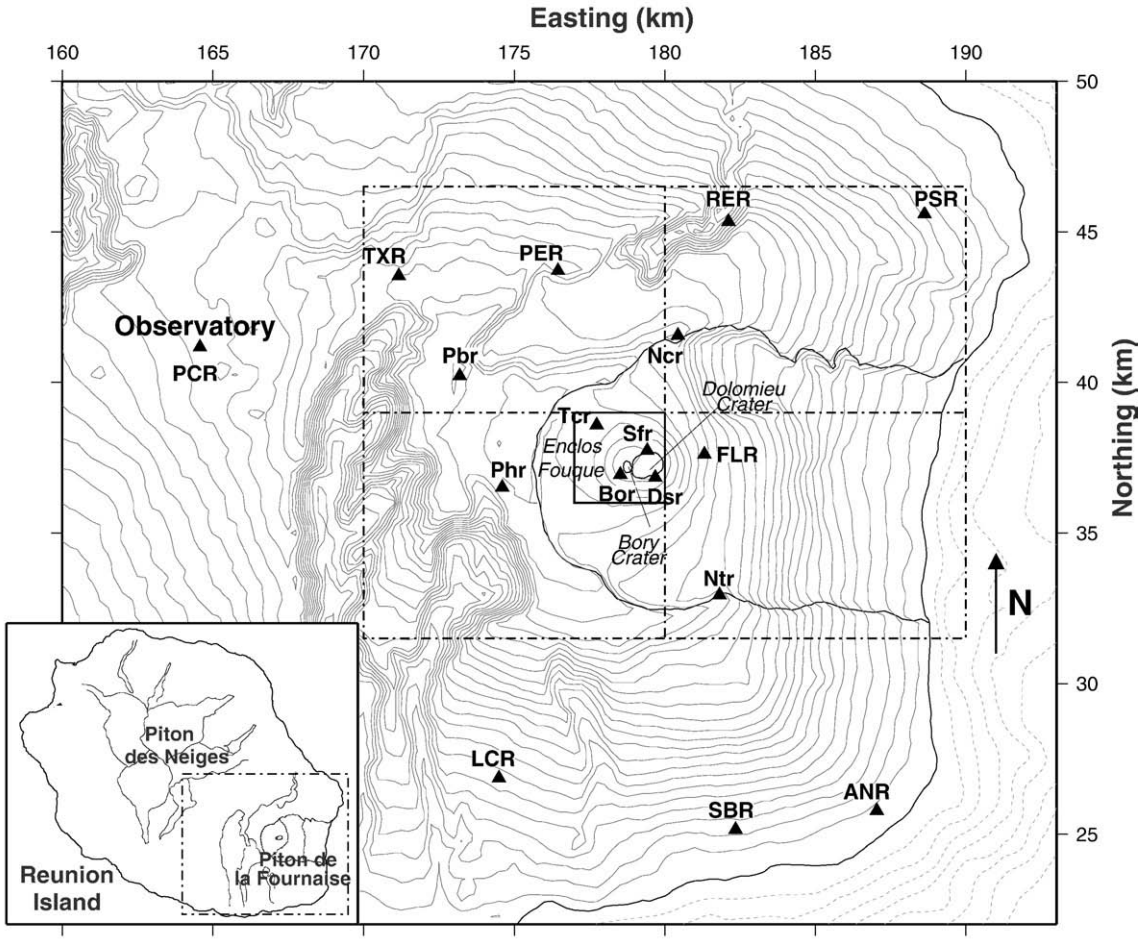


**Fig. 1.** Map of the eastern part of Réunion Island with the 13 seismic stations of the monitoring network used in this study represented as triangles. Isolines are spaced every 200 m and geographical coordinates are Gauss-Laborde kilometric coordinates. The limits of the global grid (dot-dashed line) and local grid (black line) used for tomography are also shown.

weighted sum of the data misfit (RMS) and a penalty function (the *a posteriori* model variance):

$$(g(\mathbf{m})-\mathbf{d})^{\mathrm{T}}\mathbf{C}_{\mathbf{d}}^{-1}(g(\mathbf{m})-\mathbf{d})+(\mathbf{m}-\mathbf{m}_0)^{\mathrm{T}}\mathbf{C}_{\mathbf{m}}^{-1}(\mathbf{m}-\mathbf{m}_0) \quad (2)$$

where $\mathbf{C_d}$, $\mathbf{C_m}$ and $\mathbf{m}_0$ are respectively the data covariance matrix, the *a priori* model covariance matrix and the *a priori* model vector. Data are fitted in an iterative process using a minimal perturbation of the model, controlled by the penalty function. Using the Gauss-Newton scheme to minimize the cost function leads to write the perturbation vector $\delta\,\mathbf{m}_k=\mathbf{m}_{k+1}-\mathbf{m}_k$ at iteration $k$

$$\left(\mathbf{G}_k^{\mathrm{T}}\mathbf{C}_{\mathbf{d}}^{-1}\mathbf{G}_k+\mathbf{C}_{\mathbf{m}}^{-1}\right)\delta\,\mathbf{m}_k=\mathbf{G}_k^{\mathrm{T}}\mathbf{C}_{\mathbf{d}}^{-1}(\mathbf{d}-g(\mathbf{m}_k))+\mathbf{C}_{\mathbf{m}}^{-1}(\mathbf{m}_0-\mathbf{m}_k) \quad (3)$$

an equation which may be written as

$$\left(\mathbf{G}_k^{\mathrm{T}}\mathbf{C}_{\mathbf{d}}^{-1/2}\quad \mathbf{C}_{\mathbf{m}}^{-1/2}\right)\begin{pmatrix}\mathbf{C}_{\mathbf{d}}^{-1/2}\mathbf{G}_k\\ \mathbf{C}_{\mathbf{m}}^{-1/2}\end{pmatrix}\delta\mathbf{m}_k=\left(\mathbf{G}_k^{\mathrm{T}}\mathbf{C}_{\mathbf{d}}^{-1/2}\quad \mathbf{C}_{\mathbf{m}}^{-1/2}\right)\begin{pmatrix}\mathbf{C}_{\mathbf{d}}^{-1/2}(\mathbf{d}-g(\mathbf{m}_k))\\ \mathbf{C}_{\mathbf{m}}^{-1/2}(\mathbf{m}_0-\mathbf{m}_k)\end{pmatrix}. \quad (4)$$

Therefore minimizing Eq. (2) is equivalent to solving iteratively the system:

$$\begin{pmatrix}\mathbf{C}_{\mathbf{d}}^{-1/2}\mathbf{G}_k\\ \mathbf{C}_{\mathbf{m}}^{-1/2}\end{pmatrix}\delta\mathbf{m}_k=\begin{pmatrix}\mathbf{C}_{\mathbf{d}}^{-1/2}(\mathbf{d}-g(\mathbf{m}_k))\\ \mathbf{C}_{\mathbf{m}}^{-1/2}(\mathbf{m}_0-\mathbf{m}_k)\end{pmatrix}. \quad (5)$$

Solving Eq. (5) implies the computation of $\mathbf{C}_{\mathbf{m}}^{-1/2}$, whose total number of elements (the square of the number of parameters) may be as high as $10^{12}$. To avoid the inversion of $\mathbf{C_m}$, Monteiller et al. (2005) designed a fast and accurate direct approximation of $\mathbf{C}_{\mathbf{m}}^{-1/2}$ in the case where the correlation between velocity parameters (located respectively at positions $\boldsymbol{\rho}$ and $\boldsymbol{\rho}'$) is expressed by the $L_1$-norm correlation function:

$$\mathbf{C}_v(\boldsymbol{\rho},\boldsymbol{\rho}')=\sigma_v^2 e^{\frac{-|\boldsymbol{\rho}-\boldsymbol{\rho}'|}{\lambda}} \quad (6)$$

where $\sigma_v^2$ is the variance of the velocity for the node located at $\boldsymbol{\rho}$, and $\boldsymbol{\lambda}$ is a correlation length.

The rapid solution of Eq. (5) allows the exploration of numerous values of $\boldsymbol{\lambda}$ and $\sigma_v$ and the choice of an optimal quantity of a priori information and an optimal model. The solution remains stable even when the data constrain poorly the model. We discuss hereafter the choice of the optimal parameters $\boldsymbol{\lambda}$ and $\sigma$ for our tomographic setting. Notice that minimizing the cost function (Eq. (2)) rather than only the misfit function ensures that the model found is the simplest possible: its variation from the *a priori* knowledge is minimal in amplitude and in number of independent parameters.

## 5. Model description

### 5.1. Volume of interest

In the tomography program which we use, each velocity model is described by a 3D grid of regularly spaced nodes on which the P-wave

Please cite this article as: Prôno, E., et al., P-wave velocity structure of Piton de la Fournaise volcano deduced from seismic data recorded between 1996 and 1999, J. Volcanol. Geotherm. Res. (2009), doi:10.1016/j.jvolgeores.2008.12.009

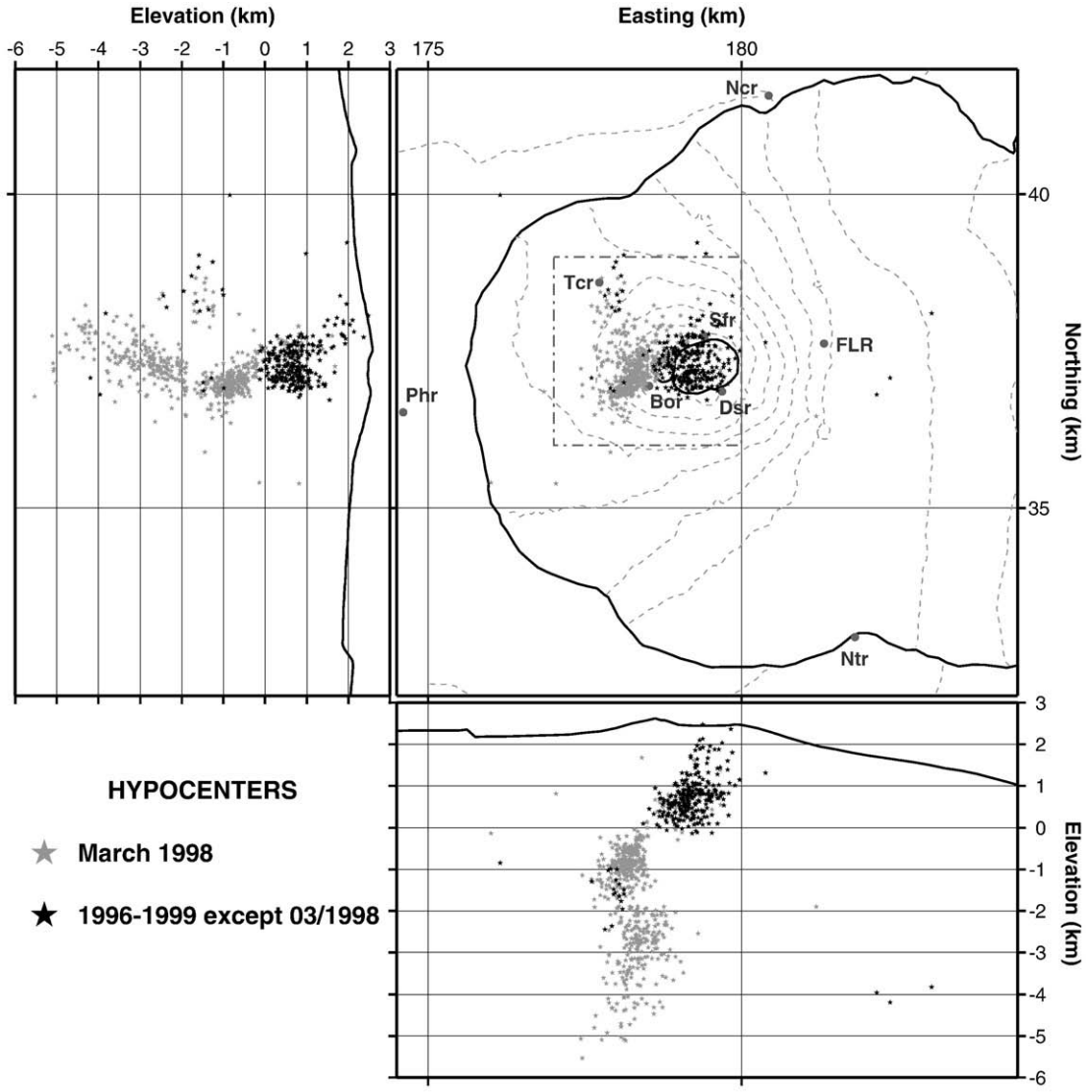


**Fig. 2.** Location of the 861 volcano-tectonic events recorded between 1996 and 1999 used for our tomographic study. The events which occurred during the March 1998 pre-eruptive swarm are shown in grey (574 events) and the other events are shown in black (287 events). Map view and north-south and east-west cross-sections are presented. The position of the local tomography grid is shown on the horizontal cross-section.

velocity is computed. To study the structure of the volcano, we consider two grids with different sizes: a large one covering the entire volcano and a smaller one close to its summit. The origin of the large grid, situated in its the middle, is located in the Enclos Fouqué at 3 km in the NNE of the Piton de la Fournaise summit (Gauss-Laborde coordinates: 39 km N, 180 km E, 0 km a.s.l.) (Fig. 1).

We first compute a P-wave velocity model at the scale of the volcano (10-km scale), hereafter referred as the global grid. It includes all source-station paths. This grid is 15 km NS, 20 km EW and 10 km in depth. We use a spatial sampling of 500 m horizontally and 250 m vertically. We also define a second, denser grid near the center of the global grid (Fig. 1) whose purpose is to provide a more precise image in the area where the resolution is the best. It is 3 km large in both NS and EW directions and 7 km vertically. It is hereafter referred as the local grid. In this grid the spatial sampling is 100 m both horizontally and vertically. Each tomography run on a local grid is preceded by a run on the global grid. The starting velocity model of the local tomography is then extracted from the 3D velocity model resulting from the global run.

To allow a precise computation of travel times by solving the eikonal equation with a finite difference algorithm, the 2 previous tomographic grids are re-sampled using tri-linear interpolation. For both local and global grids, these "fine" grids are sampled with a 50 m spacing in all directions.

### 5.2. Model parameters

It is possible with tomography to obtain a whole range of solutions that will fit equally well a given data set. The choice of the best model in that range is done by choosing the result with the lower degree of freedom (Akaike, 1974; Tarantola and Valette, 1982), i.e. the simplest model. Among the settings which have an important influence on the final tomographic model are the parameters which control the inversion procedure. In present paper we use a procedure which uses "interpretable" parameters: the correlation length and the uncertainties on the different *a priori* parameters. We tested various values for those parameters to determine their optimal values.

We consider that there are no physical reasons for two neighboring samples to be totally uncorrelated, what is expressed by the correlation function (Eq. (6)). Correlation length is a scaling parameter controlling the shape of this correlation function. Correlation of velocity parameters should not be confused with smoothing. The probabilistic algorithm which we use produces sets of solution models, and correlation acts as a stack of these models, enhancing the deterministic part relative to the

Please cite this article as: Prôno, E., et al., P-wave velocity structure of Piton de la Fournaise volcano deduced from seismic data recorded between 1996 and 1999, J. Volcanol. Geotherm. Res. (2009), doi:10.1016/j.jvolgeores.2008.12.009

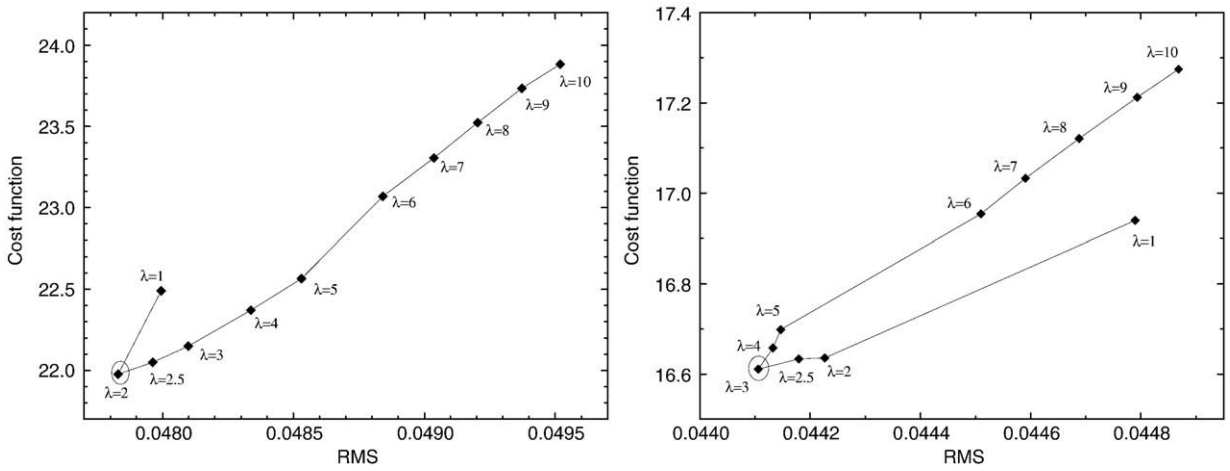


**Fig. 3.** Plot of the cost function versus the RMS for values of λ between 1 and 10 for the global (left plot) and local (right plot) grids. The curves show a turning point corresponding to a minimum of both RMS and Cost function for λ = 2 for the global grid and λ = 3 for the local grid with λ expressed in units of grid spacing. This corresponds to λ = 1000 m horizontally and 500 m vertically for the global grid and λ = 300 m in all directions for the local grid.

random part. Data misfit (RMS) and cost function both show a minimum as a function of the correlation length λ (and therefore a turning point in Fig. 3). This minimum corresponds to the optimal correlation length, and therefore to the optimal velocity model for the chosen standard deviation. We obtained a minimum of the RMS and cost function for λ = 2 on the global grid and λ = 3 on the local grid (Fig. 3) with λ expressed in units of grid spacing. This corresponds to λ = 1000 m horizontally and 500 m vertically for the global grid and λ = 300 m in all directions for the local grid.

To control the variability of the different parameters in the inversion process we assign standard deviations to each of them. These parameters are namely the velocity of the inversion cells and the position and the initial time of the earthquakes. RMS and cost function vary with both standard deviations on the hypocenter location ($\sigma_h$) and on velocity parameters ($\sigma_v$) (Figs. 4 and 5). We choose for our final tomographic models the lowest values of these standard deviations that minimize both RMS and cost functions: $\sigma_h$ = 8 km and 10 km for hypocenters respectively in the local and global grid, and $\sigma_v$ = 5 km/s for velocity parameters, for both grids. Standard deviation on the origin time has little influence and is kept to a nominal value of $\sigma_t$ = 1 s.

### 5.3. Initial velocity model

The choice of the initial velocity model was done in several steps. We first made a tomography run on the global grid with the optimal *a priori* information parameters, using as an initial model the P-waves velocity model used for routine location at the OVPF. This model includes 8 layers with constant velocities (Fig. 6). The run provided a 3D model which we used to define a 1D mean velocity model. This model was calculated by stacking vertical velocity profiles extracted from the obtained P-velocity grid. The stacking was done using profiles for all nodes in the central part of the grid where the resolution is the best from -3 km to +3 km in the NS and EW directions. The obtained mean velocity profile (Fig. 6) shows some notable velocity anomalies with depth. However to avoid using an unusefully complex model as a starting 1D model for tomography, we performed a linear adjustment of the average velocity model with depth, which provides us a constant-gradient initial model used later in this paper (Fig. 6).

## 6. Resolution tests

The size of the parameter space is too large to compute directly the resolution matrix and the uncertainty for each velocity parameter. Therefore various synthetic tests have been carried out to determine where the obtained velocity models are well constrained and therefore which features are reliable. We performed both local scale (spike) and global scale (checkerboard) tests. Checkerboard tests allow to represent the spatial extent of interpretable results, and spike tests are used to estimate the resolution of each velocity parameter in a limited volume. Each test is carried out in a similar way as a 3-stage

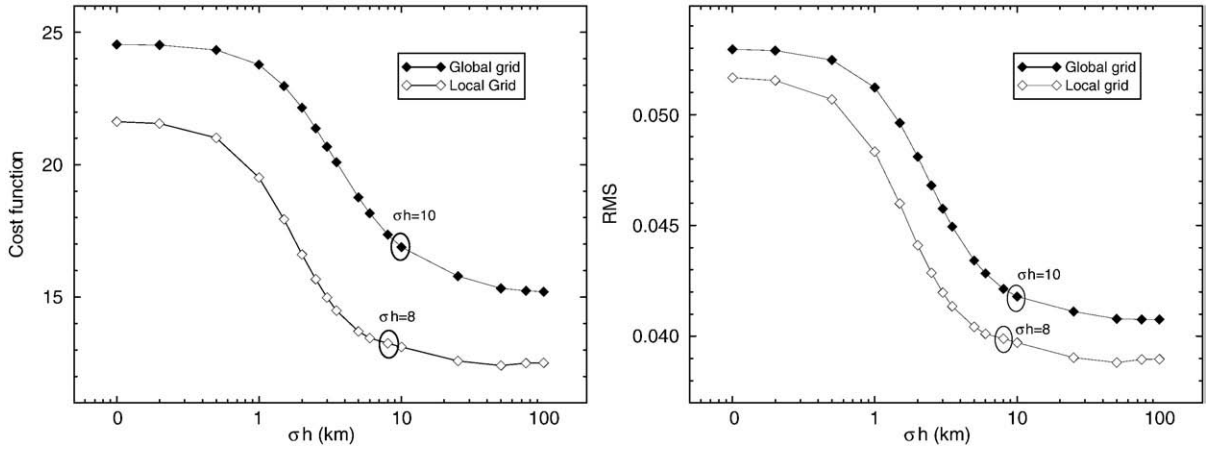


**Fig. 4.** Plot of the cost function and RMS as a function of $\sigma_h$ for values of $\sigma_h$ between 0.1 and 100 km (logarithmic scale). The curves show a minimal plateau that starts at $\sigma_h$ = 10 km for the global grid and $\sigma_h$ = 8 km for the local grid.

Please cite this article as: Prôno, E., et al., P-wave velocity structure of Piton de la Fournaise volcano deduced from seismic data recorded between 1996 and 1999, J. Volcanol. Geotherm. Res. (2009), doi:10.1016/j.jvolgeores.2008.12.009

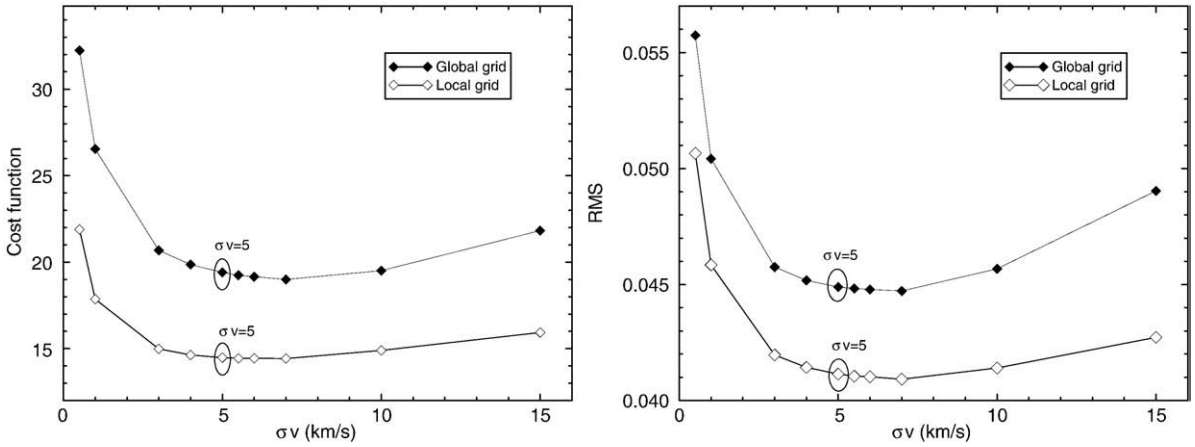


**Fig. 5.** Plot of the cost function and RMS versus $\sigma_v$ for values of $\sigma_v$ between 0.5 and 15 km/s. The curves show a minimal plateau that starts at $\sigma_v$=5 km/s for both the global and the local grid.

process: (1) a velocity anomaly is added to the final velocity model, (2) synthetic travel times are calculated in the perturbed model for the available station/event configuration and (3) the synthetic travel times are inverted starting from the initial constant-gradient model. The inversion is carried out using the same inversion and grid settings as for tomography but keeping the position and origin time of the sources fixed.

### 6.1. Checkerboard tests

The checkerboard test is the reconstruction of a checkerboard-like velocity model from the synthetic travel times computed in this model. The reconstruction is successful where the tomographic cells (velocity parameters) are sampled by enough secant source-stations paths. The synthetic velocity model was built by applying weak, spatially periodic, positive and negative anomalies of (i) 200-m/s amplitude, 4-km wavelength in the volume of the global grid, (ii) 50-m/s amplitude, 2-km wavelength in the volume of the local grid. Synthetic travel times were computed in these models.

Results of the checkerboard tests show the volume in which the ray path distribution allows the reconstruction of the model (Figs. 7–9) and therefore limits the volume of interest depending on the data set used. Vertical cross-sections of the recomposed checkerboards for the global and local grids indicate a rather good reconstruction of the medium along the more or less vertical conduit defined by the seismicity below the summit caldera. Away from the conduit the resolution strongly drops, due to the poor ray coverage in those volumes. Results indicate that the synthetic model may be reconstructed in the close vicinity of the seismic swarm below the summit from 2 km a.s.l. To 3.5 km b.s.l. depth (Figs. 7–9). The data mainly allow the reliable reconstruction of a 1D velocity model below the summit.

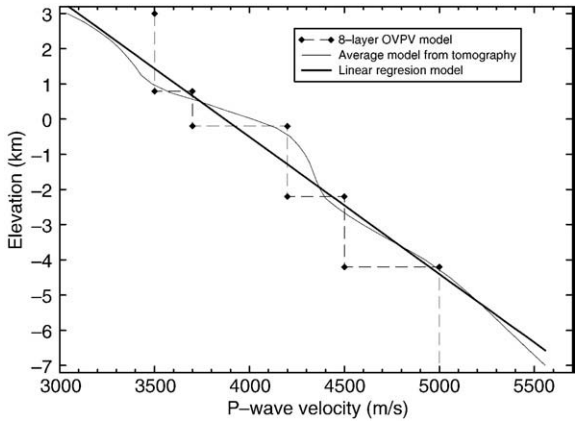


**Fig. 6.** One-dimensional velocity models: 8 layer velocity model used as a starting model for a preliminary tomography run (dashed line), average velocity model calculated over vertical profiles extracted in the well resolved part of the 3D tomography model obtained from the preliminary run (black thin line) and linear regression (thick black line) calculated using the average model. The linear model is used as a starting model for the tomography run whose results are presented in the paper.

### 6.2. Spike test

The spike test is the reconstruction of one velocity parameter embedded in an elsewhere homogeneous model. Iterative reproduction of this test for each velocity parameter of the (limited) volume of interest, gives a good outline of the resolution matrix in this volume. The amplitude of the one-parameter velocity variation used in the present study is +500 m/s. This test was repeated on the global grid with a one-kilometer spacing on 252 nodes of our volume of interest: 6 nodes NS (35 to 40 km), 6 EW (176 to 181 km) and 7 vertically (−2 to 4 km depth). The amplitude of the restored spikes reaches 70% for the best resolved node (at 1 a.s.l. depth, below the summit) and decreases with the distance from the seismic swarm and depth (Fig. 10).

## 7. Modeling results

### 7.1. Three dimensional results

We present 3D velocity models obtained for the local and global grids with the optimal *a priori* information parameters determined above for $\sigma_h$, $\sigma_v$, $\sigma_t$ and $\boldsymbol{\lambda}$. We used 861 events recorded by at least 4 stations, providing 7965 P-wave first arrival times. The tomographic inversion is started from the 1D velocity model defined previously for the global grid and the iterative process is stopped after 10 iterations since no significant reduction of the time residuals is obtained after. For the local grid, 10 iterations are also processed starting from the 3D model obtained for the global grid.

The global volume spans 15 x 20 x 10 km, that is 3000 km$^3$ sampled by 52,111 nodes (500-m horizontal, 250-m vertical sampling interval). This global grid includes at the surface the Enclos Fouqué, the 13 OVPF seismic stations which we use and the hypocenters of the 861 located events (Fig. 11). The local volume spans 3 x 3 x 8 km, that is 72 km$^3$ sampled by 77,841 nodes (100-m sampling interval). This local volume includes at the surface the summit craters of the Piton de la Fournaise (Bory in the west and Dolomieu in the east) and 4 seismic stations. It is

Please cite this article as: Prôno, E., et al., P-wave velocity structure of Piton de la Fournaise volcano deduced from seismic data recorded between 1996 and 1999, J. Volcanol. Geotherm. Res. (2009), doi:10.1016/j.jvolgeores.2008.12.009

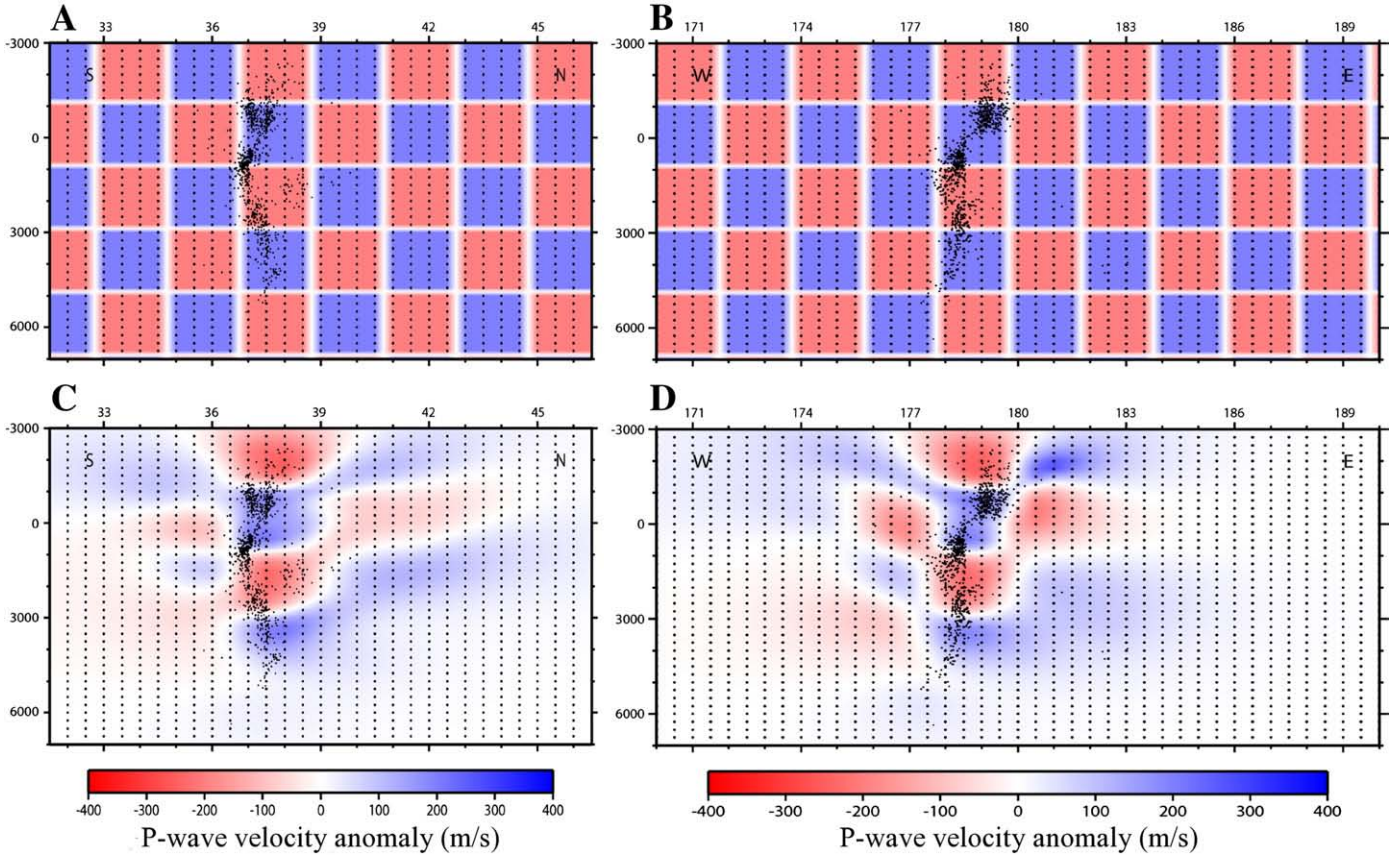


**Fig. 7.** Vertical cross-sections showing results of the checkerboard test for the global grid. Plots A and B show the initial model with velocity perturbations of ±200 m/s on 2-km wide cells. Plots C and D show the result of the tomographic inversion obtained using the synthetic travel times computed in the perturbed model. Cross-sections are made at 1500 m west of the center for the north-south section (A and C) and 1500 m south of the center for the west-east section (B and C)).

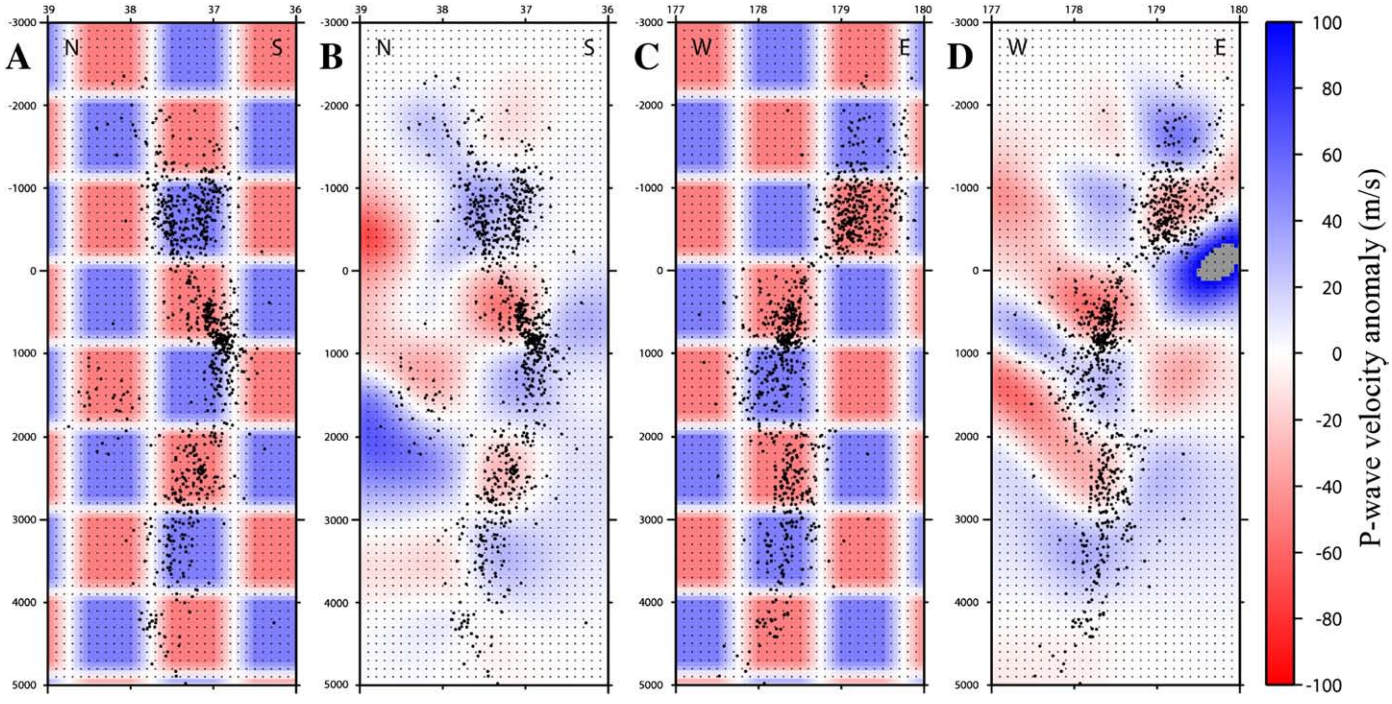


**Fig. 8.** Vertical cross-sections showing results of the checkerboard test for the local grid. Plots A and C show the initial model with velocity perturbations of ±50 m/s on 1-km wide cells. Plots B and D show the results of the tomographic inversion obtained using the synthetic travel times computed in the perturbed model. Cross-sections are made at the center of this grid, that is 1500 m west of the center of the global grid for the north-south section (A and B) and 1500 m south of the center of the global grid for the west-east section (C and D)).

Please cite this article as: Prôno, E., et al., P-wave velocity structure of Piton de la Fournaise volcano deduced from seismic data recorded between 1996 and 1999, J. Volcanol. Geotherm. Res. (2009), doi:10.1016/j.jvolgeores.2008.12.009

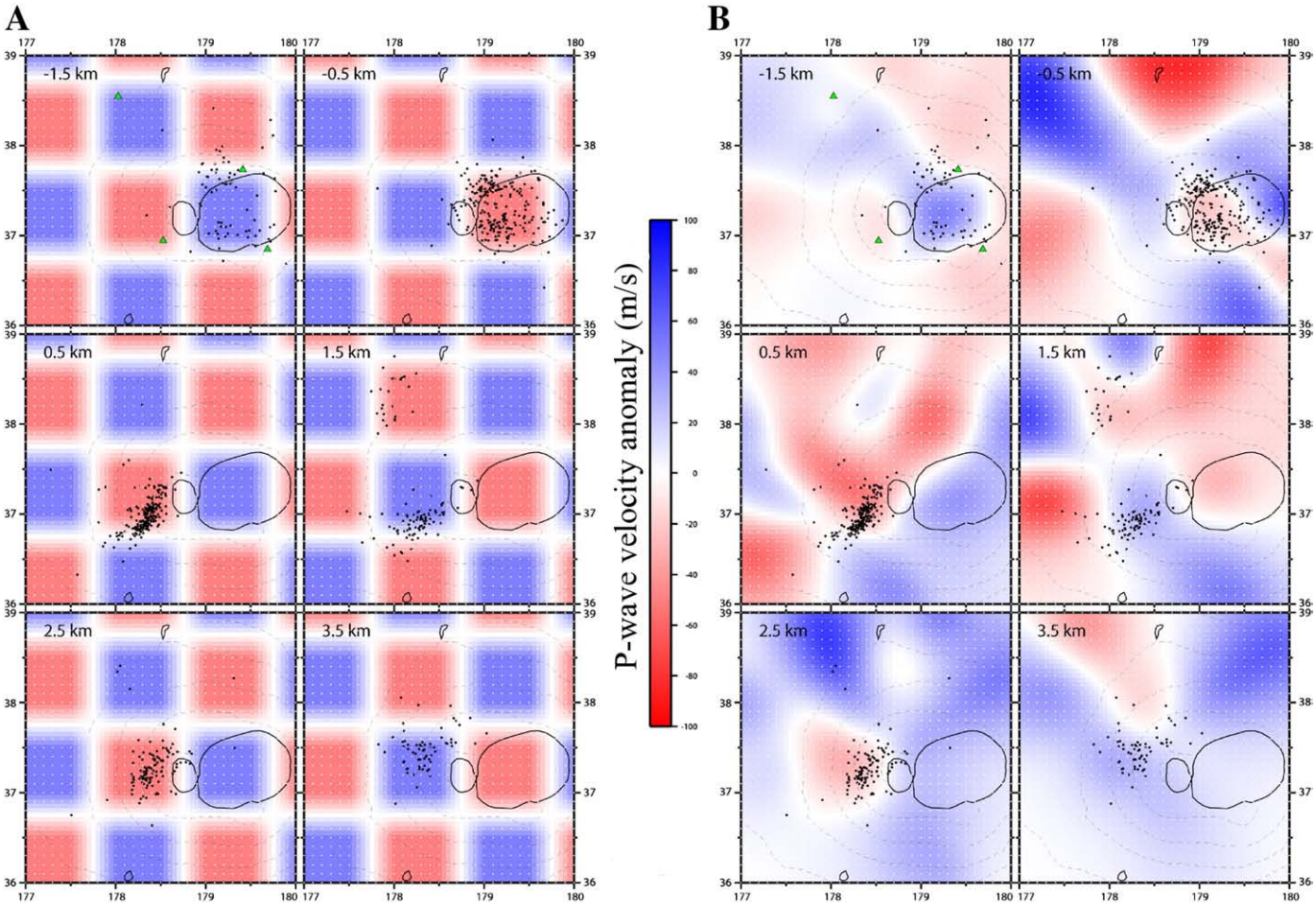


**Fig. 9.** Horizontal sections of the checkerboard test for the local grid. Plot A shows the initial model with perturbations of ±50 m/s on 1-km wide cells. Plot B shows the result of the tomographic inversion of synthetic travel times computed for the perturbed model. Cross-sections are made every 1-km depth from 1.5 km a.s.l. to 3.5 km b.s.l.

approximately centered on the seismic swarms (Fig. 12). Checkerboard and spike tests indicate that in both volumes the model is mostly well resolved in the vicinity of the earthquake swarms between 2.0 km a.s.l. and 3.5 km b.s.l.

Models are found to be stable as similar results are obtained for various inversion parameters chosen in the vicinity of the optimal parameters. Figs. 11 and 12 show horizontal and vertical cross-sections of the obtained 3D velocity models for the global and local grids, with cells not sampled by any ray shown in lighter colors. They outline remarkable systematic features indicating a relatively complex structure whose main features are as follows. (1) Between the topographical surface and 1 km a.s.l., a high velocity volume (4.0 km/s) is observed below the central craters surrounded by lower (3.2 km/s) velocity terranes (Fig. 12C). These features have been previously observed by Nercessian et al. (1996). Fig. 12A suggests a continuation of this anomaly north of Dolomieu where the velocity is maximum (up to 4.3 km/s) and a general NS extension of the anomaly. (2) Below this volume, between 1 km a.s.l. and sea level a relatively low velocity area is observed in which most of the seismicity above sea level occurs. This low velocity volume was also identified by Nercessian et al. (1996) who could not, however, identify the lateral and lower boundaries. Our results suggest that the lateral extent of this layer appears to be greater than that of the high velocity anomaly situated above and that its lower boundary is found at sea level. (3) Sea level corresponds to an area of rapid velocity transition in the vertical direction particularly clear in the EW vertical cross-section of Fig. 12. A layer at about 3.8 km/s with a thickness of about 500 m is observed at that depth. Sea level also corresponds to a level of low seismicity as well as to an interface in the migration of the seismicity during the March 8–9, 1998 pre-eruptive crisis (Battaglia et al., 2005). (4) Below sea level, between 1 and 2 km b.s.l., a low velocity zone is observed at about 4.0 km/s. This zone of 1 km in diameter is limited to the south and west by the main swarm of earthquakes. It is at 1.5 km south and west of the center of the grid, in a zone of lower seismicity (between 1.5 and 2.0 km b.s.l.). Fig. 12A, outlines a SW-NE extension of the anomaly, similar to the extension of the hypocenters located during the 1998 swarm around 1 km b.s.l.

### 7.2. Variability of the 1D mean velocity model

An important information provided by our tomographic inversion is the vertical variation of the velocity as a function of depth below the summit caldera. Therefore to examine the dependence of the obtained models upon the inversion parameters, we processed 18 tomographic runs using different values for the inversion parameters chosen in the vicinity of the optimal parameters: $\boldsymbol{\lambda}$ equal to 2 and 3 grid nodes (physical value depends on local or global grid and direction), $\sigma_h$ equal to 3 km , 5 km and 8 km and $\sigma_v$ equal to 3 km/s, 5 km/s and 7 km/s. All runs started from the same 1D linear velocity model defined previously and include 10 iterations on the global grid followed by 10 iterations on the local one. For this range of parameters, RMS and cost functions have

Please cite this article as: Prôno, E., et al., P-wave velocity structure of Piton de la Fournaise volcano deduced from seismic data recorded between 1996 and 1999, J. Volcanol. Geotherm. Res. (2009), doi:10.1016/j.jvolgeores.2008.12.009

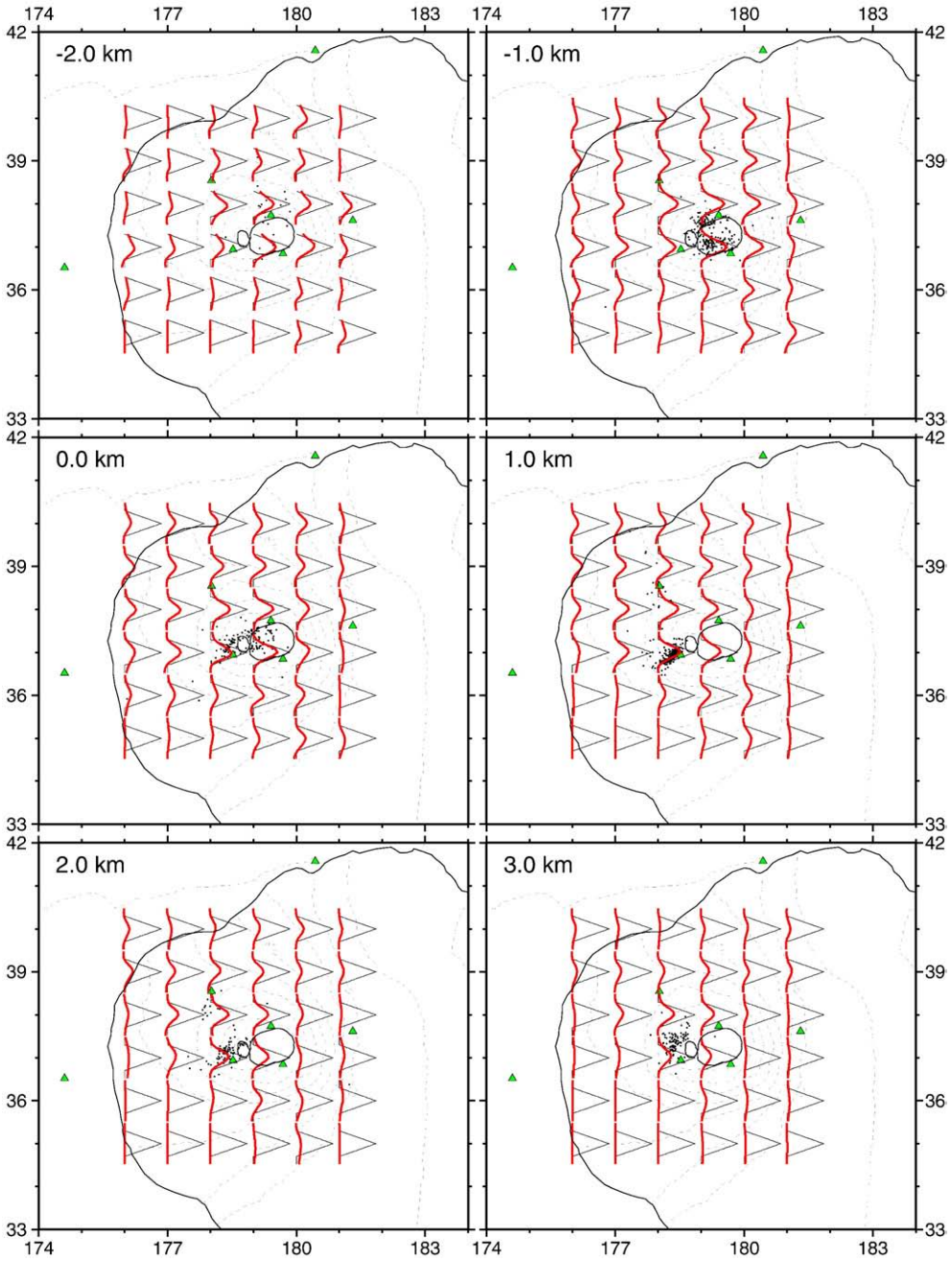


**Fig. 10.** Horizontal sections showing the restitution of spike tests at different locations of the global grid. Results are represented as vertical anomaly profiles plotted at the node where the anomaly was introduced. The introduced anomalies are represented as thin black lines, the reconstructed anomalies are in red. Spikes are scaled to avoid overlapping.

comparable values ranging respectively from 0.039 s to 0.042 s and from 13.164 to 15.066. For each tomographic run the mean vertical profile is calculated over all the nodes of the local grid.

All final mean models show similar variations. Results presented in Fig. 13 show the average profile, calculated over the 18 mean vertical profiles corresponding to each combination of parameters, and its standard deviation, as well as envelopes of the highest and lowest velocities obtained for each depth. The variability of the results is higher close to the surface and at depth where the obtained models are less constrained. Fig. 13 exhibits stable and clear average features of the velocity model just below the summit caldera. Below the high velocity superficial levels (1.5–2.5 km a.s.l.), a clear (−10 to −15%) low velocity volume appears at 0–1 km a.s.l.. These low velocities are evidenced in well-resolved volumes (Figs. 8–10) and are therefore reliable features of the model. This low velocity volume is remarkable since such zones are often difficult to image using first-arrival travel time tomography. This result has been made possible by the favorable distribution of earthquakes along the magma conduit, and the presence of seismic stations immediately in and around the summit caldera.

At the sea level, the P-wave seismic velocity strongly increases and jumps from 3.3 km/s at 0.5 km a.s.l. to 4.2 km/s at 1 km b.s.l.. Below 1.5–2. km b.s.l., the velocity is in average ~5% lower than the corresponding velocity in the initial model.

### 7.3. Earthquake locations

The earthquakes relocated in the 3D velocity structure are generally more clustered as compared to the original locations. Above

Please cite this article as: Prôno, E., et al., P-wave velocity structure of Piton de la Fournaise volcano deduced from seismic data recorded between 1996 and 1999, J. Volcanol. Geotherm. Res. (2009), doi:10.1016/j.jvolgeores.2008.12.009

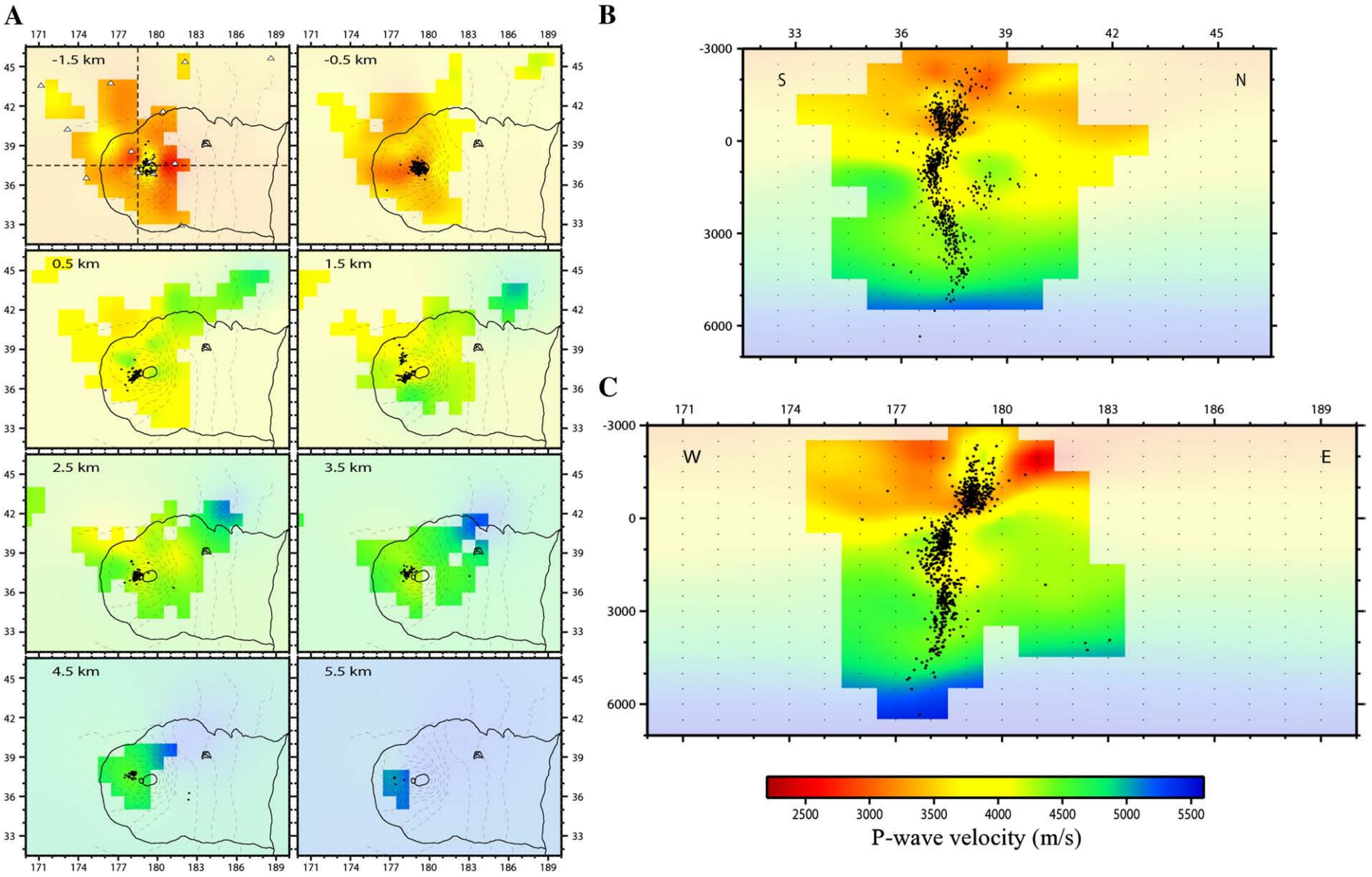


**Fig. 11.** 2D sections of the P-wave velocity model obtained for the global grid. Plot A shows horizontal sections extracted every kilometer: black points indicate the seismic hypocenters located at ±500 m from the depth of the section, white triangles in the first map indicate the location of the seismic stations, dotted lines are the location of the vertical cross-sections. Spatial coordinates are in Gauss-Laborde kilometric scale. Plot B shows the north-south vertical section and plot C the west-east section close to the principal seismic swarm. Black points indicate all the hypocenters contained in the global grid.

Please cite this article as: Prôno, E., et al., P-wave velocity structure of Piton de la Fournaise volcano deduced from seismic data recorded between 1996 and 1999, J. Volcanol. Geotherm. Res. (2009), doi:10.1016/j.jvolgeores.2008.12.009

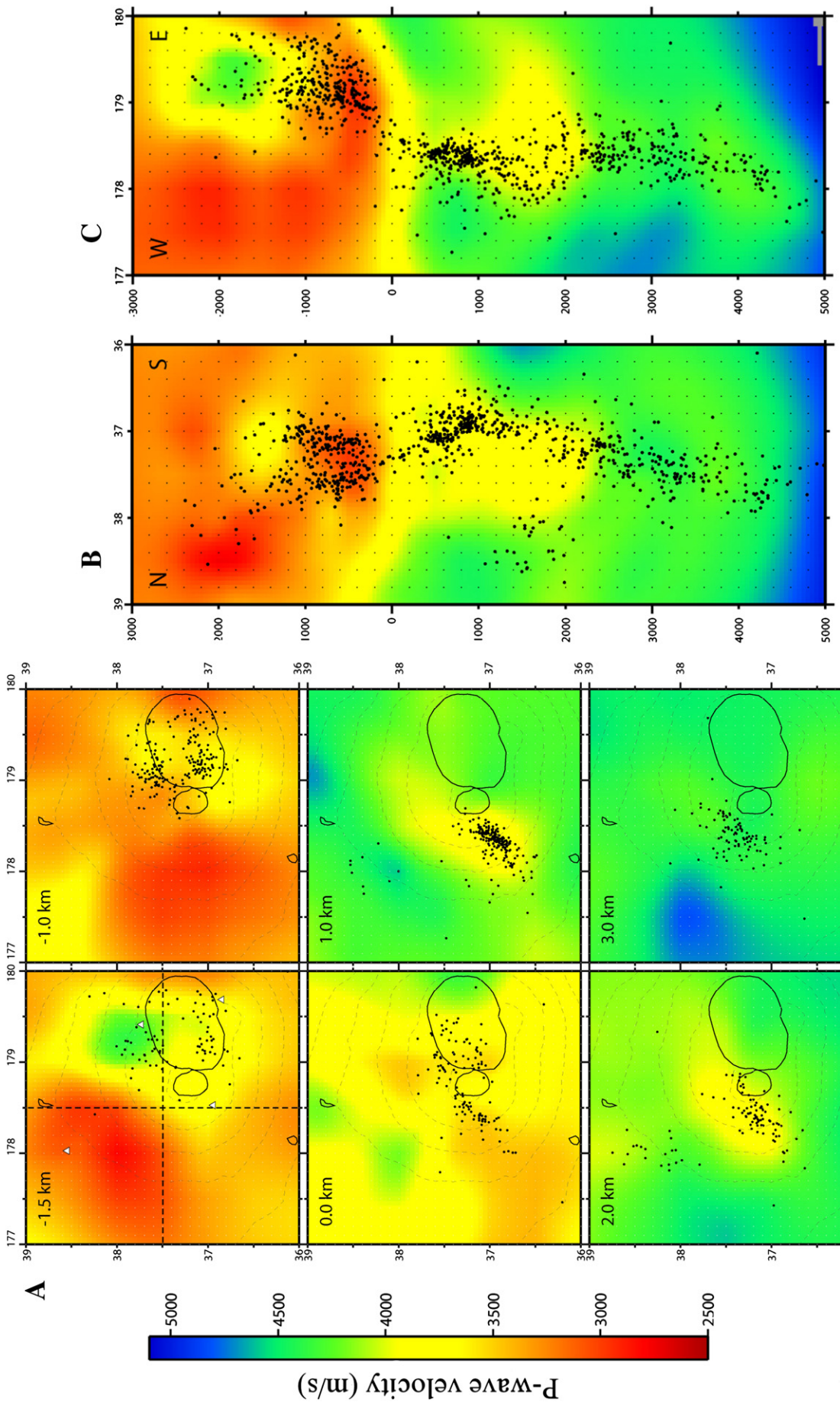


**Fig. 12.** 2D sections of the tomographic results for the local grid. Plot A shows horizontal sections extracted every kilometer. Plot B shows the north–south vertical section and plot C the west-east section taken close to the principal seismic swarm as indicated on the horizontal section at −1.5 km in plot A.

Please cite this article as: Prôno, E., et al., P-wave velocity structure of Piton de la Fournaise volcano deduced from seismic data recorded between 1996 and 1999, J. Volcanol. Geotherm. Res. (2009), doi:10.1016/j.jvolgeores.2008.12.009

sea level, they outline an interesting feature as the hypocenters align along two planar features with almost EW orientations, roughly parallel to the north and south borders of Dolomieu. These are located between 0.2 and 1.2 km a.s.l., below the Dolomieu crater and the central high velocity plug. They occur in a layer with a relatively low velocity particularly apparent in Fig. 13 as its lateral spreading is wide. The presence of such planar patterns was already identified by Sapin et al. (1996) for the period between 1985 and 1988. Our results indicate that this pattern is persistent with time.

## 8. Discussion

Our results show that P-wave velocity increases with depth from about 3.2 km/s at the top of the Piton de la Fournaise to 5.3 km/s at 6 km b.s.l. (Fig. 11). However, the velocity gradient is far from being constant as indicated by average velocity models in Figs. 13 and 3D velocity plots in Figs. 11 and 12 which outline the presence of several clear velocity anomalies.

Above 1 km a.s.l., the high velocity volume surrounded by low velocity terranes evidenced by our results may be interpreted as high-velocity, dense intrusive magma cooled at depth and forming a plug, surrounded by extrusive, light lava flows. This plug was formerly found by Nercessian et al. (1996) from travel-time tomography using earthquake data recorded by OVPF from 1985 to 1989. High-velocity intrusive magma cores located below eruptive centers are common in basaltic volcanoes (see, e.g., Kilauea volcano). The spatial extent of the observed anomaly is in good agreement with that of the very high amplitude self-potential anomaly observed below the summit area (Lénat et al., 2000). It is also correlated with a negative gravity anomaly observed and modeled by Gailler et al. (this volume).

Identifying low-velocity volumes below these eruptive centers is less common using travel-time tomography, as first arrivals propagate in the fast cores rather than in the low-velocity zones. Low-velocity zones are therefore less well resolved and velocity estimates are majored. Our earthquake data sample quite homogeneously the volume surrounding the probable magma conduit from 2 km a.s.l. to 4 km b.s.l., and allow to reconstruct properly the model between these limits according to synthetic resolution tests. We can therefore expect that at least the sign of the velocity perturbations is properly retrieved in this depth range. For these reasons, we think that both low-velocity zones (0–1 km a.s.l., 1–2 km b.s.l.) evidenced by our results are significant. Such low-velocity zones located in high-velocity cores in the vicinity of the magma conduit may be interpreted as the evidence of fluid magma storage at these depths.

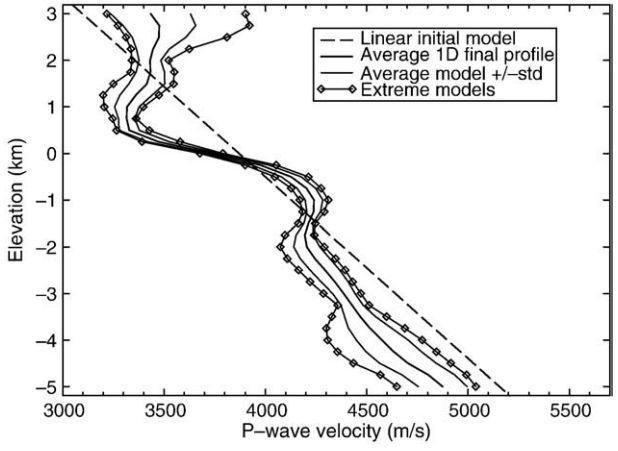


**Fig. 13.** Average 1D velocity model below the summit caldera calculated over mean models corresponding to 18 combinations of the inversion parameters chosen in the vicinity of the optimal parameters. For each of the 18 combinations, the 3D model for the local grid have been averaged over all nodes to obtain mean velocity profiles. The 18 resulting profiles have been stacked to obtain the average model (thick black line) as well as the extreme models (black lines with diamonds) and models corresponding to the standard deviation (thin black lines). The linear initial velocity model is also presented in black color.

Magma storage is thought to occur close to the surface at Piton de la Fournaise volcano according to surface deformations and partial collapses in Dolomieu crater. The occurrence of such small scale collapses like those in 1986 or 2002 may indicate that the storage system includes a significant number of shallow units, for example small pockets (sills or dykes) of magma (Lénat and Bachèlery, 1990) or temporary storages in weak zones (Longpré et al., 2007). Such pockets could be located above a larger storage system which may be at the origin of the collapse of most of the Dolomieu crater which occurred in April 2007. The small frequently observed eruptions that provoke only a superficial seismicity may indicate the partial draining of one or more of these superficial pockets located above sea level, possibly caused by some overpressure in a larger fluid storage system situated below (Sapin et al., 1996). Our results suggest that the small pockets are probably embedded in the high velocity plug while the larger storage system may correspond to one of the velocity zones evidenced below.

The distribution of earthquake hypocenters located between the sea level and the summit evokes the spatial "V" pattern with 2 divergent northward and southward branches (Fig. 12B) observed previously by Sapin et al. (1996) from the location of volcano-tectonic earthquakes recorded between 1985 and 1988. Earthquakes used in our study, which were recorded between 1996 and 1999, show a similar distribution, and confirm that this distribution is a long-lasting feature of the volcano. These branches were interpreted as due to the stress field associated with a magma chamber located below sea level. We note that according to our results these branches are situated in the low velocity zone found between 0 and 1 km a.s.l. and above a second low velocity zone found about 1–2 km b.s.l.. The two branches appear as possible fault planes for a downward sliding of the high velocity plug leading to the 2007 collapse of Dolomieu.

At sea level, our results reveal an increase in the vertical velocity gradient as P-wave velocity strongly jumps from 3.3 to 4.3 km/s within 1 km (Fig. 13). This level presents an average velocity of 3.8 km/s. It coincides with a low seismicity zone considered as a major geologic discontinuity (Battaglia et al., 2005). This discontinuity, located less than 3 km under the surface, corresponds to the position of sub-aerial lavas emitted at the beginning of the emergence of the volcano. At this level hyaloclastites and hardened deltae of lava have been evidenced (Oehler et al., 2005).

A second low velocity volume is located below the summit, at 1–2 km depth b.s.l.. This volume may be interpreted as a zone of magma storage and its depth roughly corresponds to a level of neutral buoyancy for basaltic volcanoes where the density of the magma corresponds to the density of the surrounding solid rocks (Tilling and Dvorak, 1993). The volume is also centered at a depth (1.5 km b.s.l.) which corresponds to a zone of lower seismicity (Battaglia et al., 2005). At this depth, a cluster of earthquakes was observed below station Tcr on the northern border of the low velocity zone during the 1998 pre-eruptive swarm as well as during the preceding months. This cluster, which is situated away from the main path described by the 1998 pre-eruptive hypocenters may therefore correspond to fracturation on the side of this deeper storage volume and may be related to its over-pressurization during and before the 1998 swarm. The 1998 eruption was characterized by seismicity above and below this volume prior to its onset. The rare observation of seismicity at that depth may indicate that shallower reservoirs are only periodically refilled by such deeper reservoirs as suggested by Lénat and Bachèlery (1990). The eruptions considered as exceptional from their duration or their volume (1977, 1998, 2007) can have been fed by magma from this chamber located 1–2 km b.s.l. and from deeper reservoirs. The

Please cite this article as: Prôno, E., et al., P-wave velocity structure of Piton de la Fournaise volcano deduced from seismic data recorded between 1996 and 1999, J. Volcanol. Geotherm. Res. (2009), doi:10.1016/j.jvolgeores.2008.12.009

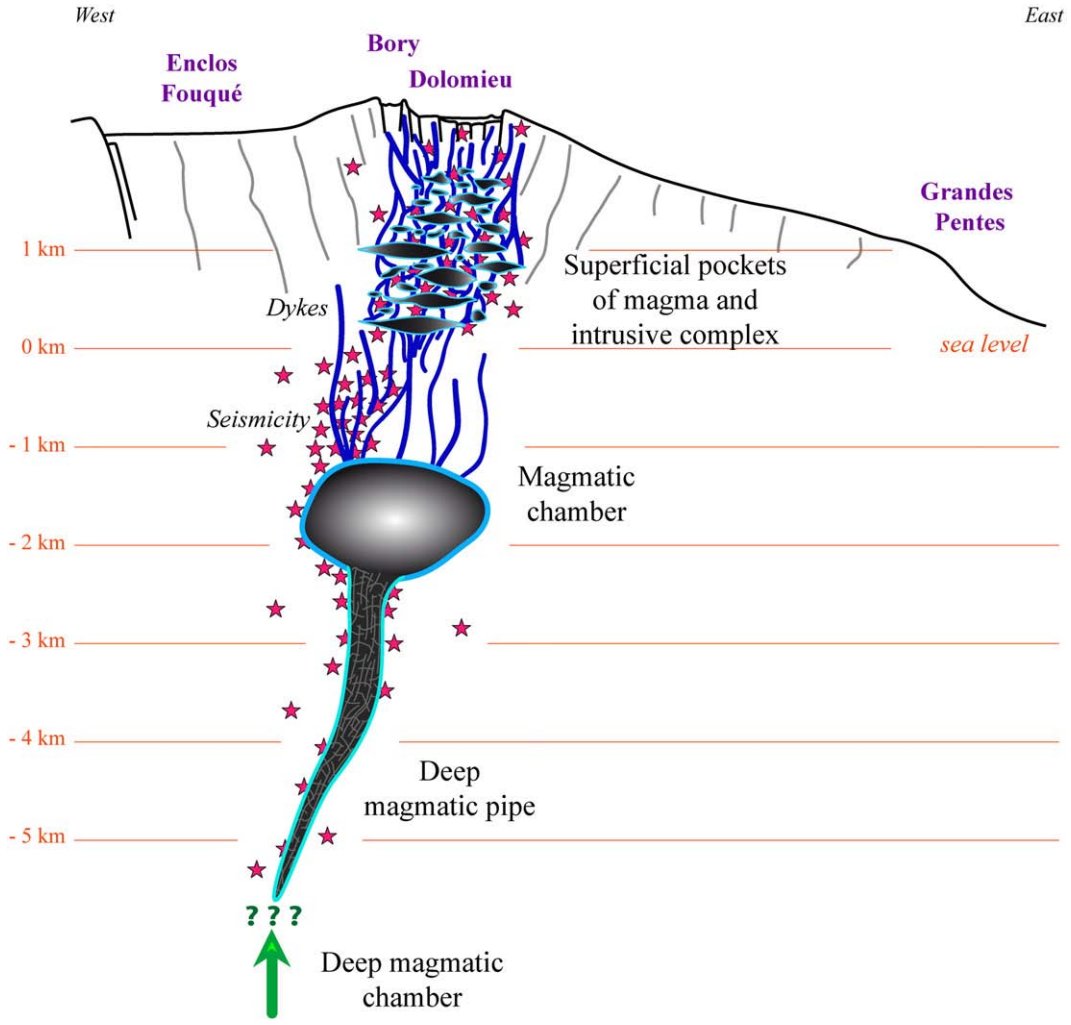


**Fig. 14.** Schematic interpretation of the tomographic results obtained using volcano-tectonic earthquakes recorded between 1996 and 1999 (modified from Lénat and Bachèlery, 1990).

different results discussed above can be summarize by the schematic figure presented in Fig. 14.

## 9. Conclusions

The objective of this work was to obtain information on the internal structure of the Piton de la Fournaise. For this purpose we proceeded with an earthquake first arrival tomographic study based on seismic data recorded by the OVPF between 1996 and 1999. Our data set included a large proportion of events located below sea level providing the opportunity to illuminate deeper structures as compared to previous tomographic works at Piton de la Fournaise.

Our study provides a P-wave velocity model which outlines several characteristic features. Synthetic tests indicate that because of the earthquake/station distribution, the final model is well resolved mostly in the vicinity of the path defined by the hypocenters and that the resolution quickly drops when going away from this path. However, the features outlined along the path appear to be stable and indicate a complex magmatic system.

The structure below the summit and above sea level appears to be composed at shallow depth of a high velocity plug surrounded by a lower velocity ring. This is interpreted as corresponding to an intrusive, solidified dyke-and-sill complex with little fluid magma storage. However, the presence of small fluid pockets in this volume is attested by the small pit craters which form occasionally in Dolomieu crater. Below the high velocity plug and above sea level, a low velocity volume is found, with a large part of the shallow seismicity located in it. This seismicity describes a V-shaped pattern with two branches having a main east–west extension, well correlated with the southern and northern borders of Dolomieu crater. The low velocity zone is limited at its bottom by an area of strong vertical velocity gradient which is found at sea level. Our tomographic results confirm that a major interface in the volcanic structure is located at sea level as already suggested by the spatio-temporal distribution of the seismicity preceding the March 1998 eruption. Below sea level, about 1–2 km b.s.l., a second zone of low velocity is observed with a low seismicity zone in its center. This could correspond to a volume of magma storage that may feed the major eruptions of the Piton de la Fournaise volcano.

## Acknowledgments

We are grateful to the staff of the Observatoire Volcanologique du Piton de la Fournaise, and especially to the Scientist-in-charge Thomas Staudacher for their help in providing high quality seismic data.

## References

Akaike, H., 1974. A new look at the statistical model identification. IEEE Trans. Autom. Contr. 19 (6), 716–723.

Aki, K., Lee, W.H.K., 1976. Determination of three dimensional velocity anomalies under a seismic array using first P-arrival times from local earthquakes. J. Geophys. Res. 81, 4381–4399.

Alfaro, R., Brandsdóttir, B., Rowlands, D.P., White, R.S., Gudmundsson, M.T., 2007. Structure of the Grímsvötn central volcano under the Vatnajökull icecap, Iceland. Geophys. J. Int. 168, 863–876.

Please cite this article as: Prôno, E., et al., P-wave velocity structure of Piton de la Fournaise volcano deduced from seismic data recorded between 1996 and 1999, J. Volcanol. Geotherm. Res. (2009), doi:10.1016/j.jvolgeores.2008.12.009

Bachèlery, P., 1981. Le Piton de la Fournaise (Ile de la Réunion): étude volcanologique, structurale et pétrologique, Thèse Univ. Clermond-Ferrand II, France.
Battaglia, J., Ferrazzini, V., Staudacher, T., Aki, K., Cheminée, J.-L., 2005. Pre-eruptive migration of earthquakes at the Piton de la Fournaise volcano (Réunion island). Geophys. J. Int. 161, 549–558.
Benz, H.M., Chouet, B.A., Dawson, P.B., Lahr, J.C., Page, R.A., Hole, J.A., 1996. Three-dimensional P and S wave velocity structure of Redoubt Volcano, Alaska. J. Geophys. Res. 101, 8111–8128.
Bonneville, A., 1990. Structure de la lithosphère. In: Lénat, J.-F. (Ed.), Le volcanisme de la Réunion. Centre de Recherches Volcanologiques, Clermont-Ferrand, pp. 1–18.
Brenguier, F., Shapiro, N.M., Campillo, M., Nercessian, A., Ferrazzini, V., 2007. 3-D surface wave tomography of the Piton de la Fournaise volcano using seismic noise correlations. Geophys. Res. Lett. 34, L02305. doi:10.1029/2006GL028586.
Gailler, L., Lénat, J.-F., Lambert, M., Levieux, G., Villeneuve, N., Froger, J.-L. Structure and change of Piton de la Fournaise inferred from gravity surveys (Réunion Island, Indian Ocean), J. Volcanol. Geotherm., this volume.
Gallart, J., Driad, L., Charvis, P., Sapin, M., Hirn, H., Diaz, J., De Voogd, B., Sachpazi, M., 1999. Perturbation to the lithosphere along the hotspot track of La Réunion from an offshore-onshore seismic transect. J. Geophys. Res. 104, 2895–2908.
Garcia-Aristizabal, A., Kumagai, H., Samaniego, P., Mothes, P., Yepes, H., Monzier, M., 2007. Seismic, petrologic, and geodetic analyses of the 1999 dome-forming eruption of Guagua Pichincha volcano, Ecuador. J. Volcanol. Geotherm. Res. 161, 333–351.
Gillot, P.Y., Nativel, P.E., 1989. Eruptive history of the Piton de la Fournaise volcano, Réunion island, Indian Ocean. J. Volcanol. Geotherm. Res. 36, 53–65.
Lee, W.H.K., Lahr, J.C., 1975. HYPO71 (revised): a computer program for determining hypocenter, magnitude, and first motion pattern of local earthquakes. U.S. Geol. Surv. Open File Rep., pp. 75–311. 10 pp.
Lénat, J.-F., Bachèlery, P., 1990. Structure et fonctionnement de la zone centrale du Piton de la Fournaise, Monographie - Le volcanisme de la Réunion. In: Lénat, J.-F. (Ed.), Le volcanisme de la Réunion. Centre de Recherches Volcanologiques, Clermont-Ferrand, pp. 257–296.
Lénat, J.-F., Fitterman, D., Jackson, D.B., Labazuy, P., 2000. Geoelectical structure of the central zone of Piton de la Fournaise volcano (Réunion). Bull. Volcanol. 62, 75–89.
Longpré, M.A., Staudacher, T., Stix, J., 2007. The November 2002 eruption at Piton de la Fournaise volcano, La Réunion Island: ground deformation seismicity, and pit crater collapse. Bull. Volcanol. 69, 511–525.
Michon, L., Staudacher, T., Ferrazzini, V., Bachèlery, P., Marti, J., 2007. April 2007 collapse of Piton de la Fournaise: a new example of caldera formation. Geophys. Res. Lett. 34, L21301. doi:10.1029/2007GL031248.
Molina, I., Kumagai, H., Le Pennec, J.-L., Hall, M., 2005. Three-dimensional P-wave structure of Tungurahua Volcano, Ecuador. J. Volcanol. Geotherm. Res. 147, 144–156.
Monteiller, V., Got, J.-L., Virieux, J., Okubo, P., 2005. An efficient algorithm for double-difference tomography and location in heterogeneous media, with an application to the Kilauea volcano. J. Geophys. Res. 110, B12306. doi:10.1029/2004JB003466.
Nercessian, A., Hirn, A., Lépine, J.-C., Sapin, M., 1996. Internal structure of Piton de la Fournaise volcano from seismic wave propagation and earthquake distribution. J. Volcanol. Geotherm. Res. 70, 123–143.
Oehler, J.-F., Van Wyk de Vries, B., Labazuy, P., 2005. Lanslides and spreading of oceanic hot-spot and arc shield volcanoes on Low Strength Layers (LSLs): an analogue modeling approach. J. Volcanol. Geotherm. Res. 144, 169–189.
Podvin, P., Lecomte, I., 1991. Finite-difference computation of traveltimes in very contrasted velocity models — a massively parallel approach and its associated tools. Geophys. J. Int. 105, 271–284.
Sapin, M., Hirn, A., Lépine, J.-C., Nercessian, A., 1996. Stress, failure and fluid flow deduced from earthquakes accompanying eruptions at Piton de la Fournaise volcano. J. Volcanol. Geotherm. Res. 70, 145–167.
Stieltjes, L., Moutou, P., 1989. A statistical and probabilistic study of the historic activity of the Piton de la Fournaise, Réunion Island, Indian Ocean. J. Volcanol. Geotherm. Res. 36, 67–86.
Tarantola, A., 1987. Inverse Problem Theory. Elsevier, New York. 613 pp.
Tarantola, A., Valette, B., 1982. Generalized nonlinear inverse problems solved using the least-squares criterion. Rev. Geophys. 20, 219–232.
Tilling, R., Dvorak, J., 1993. Anatomy of a basaltic volcano. Nature 363, 125–132.
Vanorio, T., Virieux, J., Capuano, P., Russo, G., 2005. Three-dimensional seismic tomography from P wave and S wave microearthquake travel times and rock physics characterization of the Campi Flegrei Caldera. J. Geophys. Res. 110, B03201. doi:10.1029/2004GL003102.

Please cite this article as: Prôno, E., et al., P-wave velocity structure of Piton de la Fournaise volcano deduced from seismic data recorded between 1996 and 1999, J. Volcanol. Geotherm. Res. (2009), doi:10.1016/j.jvolgeores.2008.12.009